INTERNATIONAL JOURNAL FOR NUMERICAL METHODS IN FLUIDS
Int. J. Numer. Meth. Fluids 2002; **39**:799–819 (DOI: 10.1002/fld.330)

VLES modelling of geophysical fluids with nonoscillatory forward-in-time schemes

P. K. Smolarkiewicz*,[1] and J. M. Prusa[2]

[1] *National Center for Atmospheric Research, Boulder, Colorado 80307, U.S.A.*
[2] *Iowa State University, Ames, Iowa 50011, U.S.A.*

SUMMARY

Atmospheres and oceans are mostly incompressible and turbulent. The experience of the meteorological community with modelling such flows is based primarily on centred in time and space (CTS) methods. Our experience applying non-oscillatory forward in time methods (NFT) to a range of flows has revealed some unexpected benefits specifically in the area of modelling geophysical turbulence where broad span of scales, density stratification, planetary rotation, inhomogeneity of the lower boundary, etc., make explicit modelling of subgrid-scale motions particularly challenging. It turns out that in the absence or insufficiency of a proper subgrid-scale model, NFT methods supply their own, implicit, turbulence models that are quite effective in assuring quality simulations of high-Reynolds number flows. Since such simulations abandon rigorous notion of the large-eddy simulation approach, and merely aim at computing explicitly large coherent eddies resolvable on the grid, they are referred to as very-large-eddy simulations (VLES). In this paper we will describe advantages of the NFT approach and illustrate them with an example of gravity-wave-breaking induced turbulence in a deep atmosphere. On the philosophical side, we challenge a common misconception that NFT methods are overly diffusive and therefore inadequate for high Reynolds number flow simulations. Copyright © 2002 John Wiley & Sons, Ltd.

KEY WORDS: geophysical turbulence; large eddy simulation; finite difference methods for fluids; subgrid-scale models

1. INTRODUCTION

Geophysical fluids such as atmospheres and oceans are characterized by high Reynolds number and low Mach number. This indicates that, to first approximation, they are incompressible and turbulent. As in engineering flows, turbulence in atmospheres and oceans is generated by heating and boundary stresses. Effects uncommon in engineering applications are due to planetary rotation and density/temperature stratification. Rotating stratified fluids support a variety of inertio-gravity and planetary waves. When the amplitude of the waves becomes comparable to their wavelengths, the waves break—generating a localized burst of turbulence.

* Correspondence to: P. K. Smolarkiewicz, National Center for Atmospheric Research, P.O. Box 3000, Boulder, Colorado 80307, U.S.A.

Received October 2001
Revised December 2001

The familiar pictures of white water in a mountain stream or of breaking surf on a beach are not far removed from phenomena which occur internally in geophysical flows of all scales.

The large-eddy simulation (LES) approach has a proven record in the research of turbulent atmospheric and oceanic flows. Typically, LES is understood as a numerical integration of Navier–Stokes' equations filtered appropriately such as to compute explicitly all scales of motion larger than some multiplicity of the grid interval ΔX (e.g. $2\Delta X$ [7]), whereas unresolved scales are modelled based on universal properties of fully developed turbulence; cf. Reference [27]. The intent behind LES is to account for (viz. parameterize) the subgrid-scale (SGS) motions below the available resolution of the numerical model at hand or, in other words, to account for a net effect of smallscales on those resolved on the grid. The overall idea of LES is simple and elegant, yet often difficult to realize effectively in applications. The literature on LES is vast and continuously growing—the interested reader is referred to References [23, 18, 25, 15] for reviews and discussions.

The formalism of decomposing flow variables into resolved and unresolved scales of motion leads straightforwardly to filtered equations that include on the right-hand side (RHS) terms depending on the divergence of the anisotropic component of the so-called SGS stress tensor, a combination of various products of unresolved and resolved components of the flow variables. In general, the entries of the SGS stress tensor are uncomputable and must be expressed in terms of the resolved components of the flow variables. The latter procedure forms a SGS model—a key ingredient of a successful LES; cf. Reference [15]. In meteorology, the most popular Smagorinsky SGS model postulates an SGS stress tensor proportional to the rate of strain (of the resolved flow) via a local eddy-viscosity coefficient. The eddy coefficient itself depends on the magnitude of the local strain rate. Formal SGS models are not necessarily simple, and when combined with non-orthogonal time-dependent geometries (forming a base of mesh refinement schemes) they become overly complicated and cumbersome.

Historically, the development of SGS models for meteorological codes was not motivated by physical principles of LES, but by inadequate stability of numerical solutions (viz., non-linear instability problem; [38]). Consequently, the utility of SGS models is often appreciated not for their sound representation of actual turbulence that might occur on the subgrid scales but rather as a means of suppressing false computational oscillations. However, if non-linear instability is of concern, there are simpler, more effective, and more universal means of preventing it (cf. the paragraph concluding Smagorinsky's [38] historical remarks). Numerical simulations of turbulent flows that abandon rigorous notions of LES and merely aim at explicitly computing large coherent eddies resolvable on the grid are sometimes referred to as VLES (for very-large-eddy simulations [27]).

Recently, a class of finite difference methods—non-oscillatory forward-in-time (NFT)* —have exhibited the remarkable property of representing LES/VLES without recourse to any

*With 'non-oscillatory', we shall generously label all the non-linear techniques (often referred to as monotonicity or shape-preserving, shock-capturing, or briefly, monotone schemes; e.g. total variation diminishing, TVD, flux-corrected-transport, FCT, and various flux-limited and sign-preserving schemes) that suppress/reduce/control numerical oscillations characteristic of higher-order linear schemes. After Reference [52], 'forward-in-time' (FT) labels a class of generalized one-step Lax–Wendroff type methods. Altogether, 'NFT' is meant to distinguish from classical centred-in-time-and-space (CTS) linear methods, notorious for exhibiting spurious oscillations.

explicit subgrid-scale model. In particular, Margolin *et al*. [22] demonstrated that a mesoscale atmospheric code based on the non-oscillatory advection scheme MPDATA [48] can accurately reproduce (i.e. in close agreement with field and laboratory data and the existing benchmark computations) the dynamics of the convective planetary boundary layer. When an explicit turbulence model was implemented, MPDATA did not add any unnecessary diffusion. Of greater interest, when no explicit turbulence scheme was employed MPDATA itself appeared to include an effective SGS model. Finally, with the explicit turbulence model but eddy viscosity reduced by some factor, MPDATA added just enough dissipation. Taken together, this documents the self-adaptive character of the NFT solver's dissipative properties, which appear to be physically realistic.

Several researchers have reported similar success, by simulating turbulent flows in a variety of regimes while using only non-oscillatory advection schemes to model subgrid effects. For instance, the use of non-oscillatory schemes as an implicit turbulence model has been discussed in the context of free shear flows [26], strongly compressible turbulence [29], and the development of turbulence at Rayleigh–Taylor unstable interfaces [20]. At this point there is no theory justifying this success. Since in each of the reported applications a different NFT algorithm has been used, their common ability to accurately simulate turbulent flows (as demonstrated by comparisons with data) indicates that the non-oscillatory property *per se* (rather than details of any particular algorithm) is important. We elaborate on this throughout this paper.

Our goal is to convince the reader about the utility of the NFT approach for VLES of geophysical flows, and we will present overwhelming evidence in support of this approach. However, we do recognize that this approach is not a panacea, and in particular, that there is still a need for explicit SGS models. In parallel to the reports which prize the performance of non-oscillatory methods (as sole SGS models), there are critical works that point out some deficiencies. Moin and Kravchenko [24], and Brown *et al*. [4], document convincingly inferior performance of dissipative upwind-biased methods in frictional (shear-driven) turbulent boundary-layer flow problems. In a way, this is not necessarily surprising. By definition, frictional boundary layers are thin layers adjacent to a solid wall, where effects of viscosity are important regardless of how high the Reynolds number of the flow can be (see Section 5.7 in [3]). When viscosity becomes dominant, it is only natural to expect solutions' sensitivity to details of SGS models. In this paper, we shall focus on flows away from frictional boundary layers—a convenient scenario relevant to a broad class of geophysical applications—and proceed with disregard for potential difficulties in near-wall regions. The latter problems are the subject of intense research and, hopefully, an alternative solution which combines the strengths of explicit and implicit SGS models will appear shortly with great benefit to universality, and simplicity of VLES for geophysical flows.

The paper is organized as follows. In the following section we list some general properties of NFT schemes of relevance to simulating turbulent flows. Then we summarize the NFT formulation that we have found particularly useful in geophysical applications, but still in abstraction from any specific system of the equations of motion. Only after this, we shall describe the anelastic model equations used in our studies, and outline some details of implementing our NFT approach. Then we finish with an example application: gravity-wave-breaking induced small-scale turbulence in a deep atmosphere.

2. SOME REMARKABLE PROPERTIES OF NFT SCHEMES

The basic equation underlying turbulent flows is the homogeneous continuity equation describing the transport of a non-diffusive scalar quantity. Elementary advection schemes for this equation (such as classical donor-cell, one-step Lax–Wendroff, or CTS leapfrog; see References [35] or [30], for details) yield simple, compact forms for the resulting advective fluxes. Modern NFT methods addressed in this paper yield complex fluxes that often require many equations for their representation. Nevertheless, they produce superior results with regard to stability and accuracy, and so are worth the extra effort involved.

NFT advection schemes possess enhanced computational stability because the total 'energy' ('entropy') of a sign-preserving solution is uniformly bounded in time [42]; see Appendix for further discussion. For a sufficiently small time step Δt, advection schemes can always be designed which are sign-preserving for arbitrary flows (e.g., [39–41])—thus non-oscillatory schemes exhibit non-linear as well as linear stability. These results hold if the dependent variable field ψ is of either constant or variable sign. Arguments can be further generalized (over a single time step) to a transport equation with forcings and/or sources leading to the conclusion that sign-preserving advection schemes offer *the means of controlling non-linear stability in numerical models*.

A numerical property of great importance to turbulence simulations is flow topology—or *realizability*. This means that ψ must be advected along non-intersecting numerical trajectories. This property is subtle as superficially, intersecting trajectories may give the impression of turbulent motions (see [31]). For a flow to be realizable, the flow Jacobian $J \equiv \{\partial \mathbf{x}/\partial \mathbf{x}_o\}$, with $\mathbf{x}_o$ denoting the foot of the trajectory arriving at $(\mathbf{x}(\mathbf{x}_o, t_o), t)$, must be positive and bounded, $0 < J < \infty$ (see Chapter 2 in Reference [28], for a discussion). From the latter, and the Lagrangian form of the continuity equation $\mathrm{d}\psi/\mathrm{d}t = 0$, it follows that $\psi = \psi_o J^{-1}$ with $\psi_o = \psi|_{(\mathbf{x}_o, t_o)}$ [53]. One can thus argue that assuring sign-preserving advection of ψ, via adequate limiting of the advecting flow, amounts to assuring that the numerical trajectories do not intersect. Another condition, sufficient for flow realizability within Δt, is $\mathscr{L} < 1$, where $\mathscr{L} \equiv \Delta t \|\partial \mathbf{u}/\partial \mathbf{x}\|$ is the 'Lipschitz number' [44]. Both topological constraints depend on magnitudes of local velocity derivatives, and thus point out that *limiting local derivatives* of the resolved flow (without necessarily reducing the magnitude of Δt) should improve fidelity of the simulations. Since such a limiting is also effected by filtering small, poorly resolved eddies on the grid—regardless of the formal theoretics underlying LES—SGS models act quite similarly to the limiters of non-oscillatory schemes.

Non-oscillatory advection schemes are dissipative. In practice, this means that (i) they contain both even and odd truncation-error terms in their Taylor series expansion (in contrast to CTS schemes like the leapfrog method), and (ii) they tend to dissipate (rather than conserve) the quadratic integrals ('energy' or 'entropy') of the transported variable (in contrast to CTS schemes like Arakawa-type methods [1]). By no means does dissipativity imply low accuracy—although statements in this spirit do appear in the literature every once in a while. Non-oscillatory algorithms are available for a number of existing advection schemes that take into account flow variability and multidimensionality, and typically offer uniformly second-order accurate solutions for arbitrary flows. These algorithms are particularly attractive for VLES modelling of geophysical fluids. The remarkable efficacy (i.e. accuracy versus efficiency) of the non-oscillatory methods has been argued in the literature for the last decade (see Introduction). In order to substantiate such arguments as well as to show the

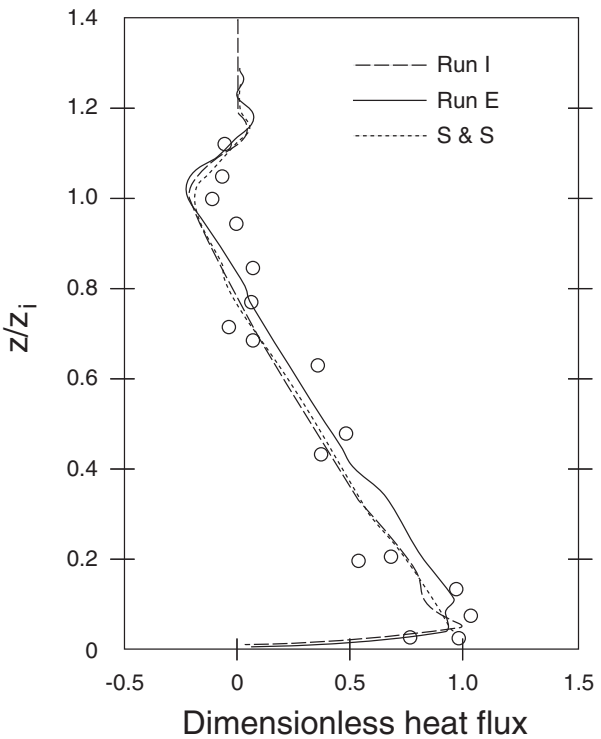

Figure 1. LES (run I) and VLES (run E) of convective PBL.

'dissipativity' at work, here we highlight the results of LES vs. VLES and DNS vs. VLES for two benchmark simulations of turbulent flows using the NFT incompressible Boussinesq model based on the MPDATA advection scheme [48].

Figure 1 highlights the simulations of convective planetary boundary layer (PBL) of Margolin *et al*. [22]. The three curves shown in the figure represent mean profiles of the resolved heat flux $\langle \theta' w' \rangle$ (normalized appropriately) from three different simulations: the short-dashed curve is from LES benchmark simulations of Schmidt and Schumann [36] using a CTS model; the long-dashed curve is from LES simulations with MPDATA, and the solid curve is for MPDATA VLES with no explicit subgrid-scale model. Circles represent field and laboratory data. The comparability of all the results with the data is excellent (for other characteristics of the flow, see [22]). Without the VLES result, one might be tempted to argue that the dissipativity of the employed NFT approach is negligibly small. However, the results shown reveal a more interesting story.

A full appreciation of the results in Figure 1 intertwines with appreciating the mechanics of non-oscillatory schemes. Such schemes are non-linear (even for linear problems) as they employ coefficients that depend on the transported variables. In other words, non-oscillatory schemes are *self-adaptive* as they design themselves in the course of the simulation. Therefore, in contrast to linear methods, different realizations of the same turbulent flow use different numerical approximations to the governing equations of motion. When the explicit SGS model

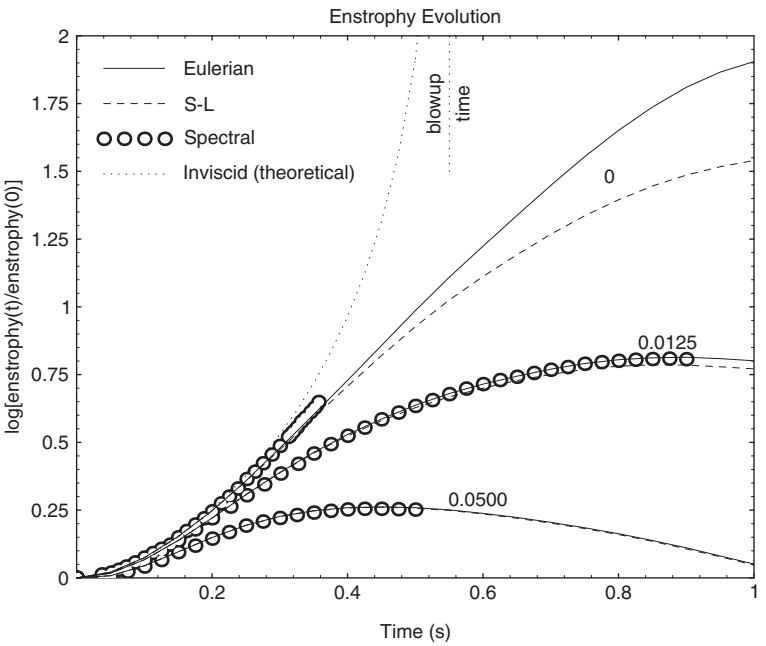

Figure 2. DNS and VLES of the decaying turbulence.

is included (LES) the resolved flow is sufficiently smooth, and the entire machinery assuring non-oscillatory properties of the numerics is effectively turned off (there is no need to limit/adjust linear components of the scheme). In the absence of an explicit SGS model (VLES) the non-oscillatory machinery adapts the numerics 'smartly' such as to assure solutions that are apparently as smooth as those generated with physically-motivated explicit SGS models. Insofar as the dissipativity *per se* of the NFT methods is concerned, there is no simple scholastic quantification, since the resulting transport scheme can be effectively either non-dissipative or dissipative, depending upon the presence or absence, respectively, of an explicit SGS model.

The second example highlights the results of DNS/VLES simulations of the decaying turbulence of a homogeneous incompressible fluid in a triply-periodic cube—a canonical problem in turbulence studies. Due to the assumed homogeneity of the thermodynamics, and the lack of near-wall effects, the focus of the problem is on the non-linearity of the convective derivatives $\mathbf{u}\nabla\mathbf{u}$ in the momentum equation, i.e. the 'categorical imperative' of the turbulence *per se*. Our NFT simulations with MPDATA (and the non-oscillatory semi-Lagrangian option of our model) follow precisely the 256^3 pseudo-spectral simulations of Herring and Kerr [13].

Figure 2 displays the numerical results for the evolution of enstrophy for three values of viscosity, $v = 0.0500$, $v = 0.0125$, and $v = 0$ m^2 s^{-1} (as indicated). Solid lines are for MPDATA experiments and dashed lines for semi-Lagrangian experiments, whereas Herring–Kerr results are marked with circles. Also shown is a theoretical estimate for inviscid flow (dotted lines)—based upon the elementary enstrophy relationship for 3D isotropic turbulence and a phenomenological model for skewness (with free parameters evaluated by matching

the numerical results at small time when viscous effects are negligible); see Chapter VI.7 in [19].

In the figure, one striking message is the remarkable agreement of the NFT and the pseudo-spectral results for DNS ($v>0$). This level of agreement is maintained uniformly throughout all flow characteristics, including spectra (see [13], for discussions and physical insights). Traditionally, pseudo-spectral methods are prized for their accuracy and considered superior tools for studying turbulent flows. Since all convergent methods eventually become accurate when the flow is fully resolved, one may wonder whether the resolution employed is an overkill. This is definitely not the case for $v=0.0125$ where the Kolmogorov scale is about one grid-interval (Kerr, personal communication) and the dissipation of the energy is not well resolved. Apparently, the NFT model employed is at least as accurate as the pseudo-spectral code. The VLES result ($v=0$) exposes the true power of the NFT approach. Without viscous dissipation, unlimited enstrophy growth is predicted; with a finite enstrophy blowup time of $t\sim 0.55$ s. With rapid enstrophy growth, the spectral calculations become computationally unstable and must be terminated after ~ 0.35 s [13]. Up to this time, the NFT, spectral, and theoretical results agree closely. After the collapse of the spectral model, the NFT computations continue but drop well below the theoretical result. This divergence is due to the flow topology condition being enforced by the NFT scheme (e.g. an implicit SGS model develops). Essentially, enstrophy has increased to the point where velocity gradients are so large that limiting of local derivatives of the flow has to be enforced for stability of the computations. Intriguingly, Figure 2 indicates that the net effect of this limiting is that the NFT scheme results in an *effective* viscosity (of $\sim 0.004\,\mathrm{m^2\,s^{-1}}$ for the Eulerian computation and approximately double that for the NFT semi-Lagrangian computation). In a sense, NFT schemes may be thought of as producing the sharpest possible (stable) LES result for an inviscid flow *for a given computational resolution*.

3. NFT METHODS FOR FLUIDS

In modelling atmospheric/oceanic flows the governing equations can always be viewed in the form of a generalized transport equation

$$\frac{\partial \rho^* \psi}{\partial \bar{t}} + \bar{\nabla} \cdot (\rho^* \bar{\mathbf{v}}^* \psi) = \rho^* R \tag{1}$$

where $\bar{\nabla} \cdot \equiv (\partial/\partial \bar{x}, \partial/\partial \bar{y}, \partial/\partial \bar{z})\cdot$ is *defined* as the divergence operator in a time variable, curvilinear coordinate system; and ψ is an intensive dependent fluid variable, e.g. component of specific momentum (viz. velocity component), potential temperature, water vapour mixing ratio, specific salinity, etc. In Equation (1), the coefficients ρ^*, $\bar{\mathbf{v}}^*$, and R are assumed to be known functions of the independent variables $(\bar{\mathbf{x}}, \bar{t})$. In anelastic-flow applications addressed in this paper, $\rho^* \equiv \rho_b \bar{G}$ plays the role of a reference density multiplied by the Jacobian of the transformation from a stationary, physical coordinate system $\mathbf{x}$ (such as Cartesian) to the curvilinear system $\bar{\mathbf{x}}$ (such as terrain-following coordinates on a rotating sphere); $\bar{\mathbf{v}}^* \equiv (\overline{u^*}, \overline{v^*}, \overline{w^*}) \equiv \mathrm{d}\bar{\mathbf{x}}/\mathrm{d}\bar{t} \equiv \dot{\bar{\mathbf{x}}}$ is the *contravariant* velocity in the curvilinear system; and R combines all forcings and/or sources. In general, both $\bar{\mathbf{v}}^*$ and R are functionals of the dependent variables (see Reference [48] for examples). With these definitions, Equation (1)

is mathematically equivalent to the Langrangian evolution equation

$$\frac{\mathrm{d}\psi}{\mathrm{d}\bar{t}} = R \tag{2}$$

regardless of the assumed form of the mass continuity equation (i.e. compressible, incompressible, Boussinesq, anelastic, etc.), with $\mathrm{d}/\mathrm{d}\bar{t} = \partial/\partial\bar{t} + \bar{\mathbf{x}}\bar{\nabla}$ for the material derivative.

Our basic NFT approach for approximating either Equation (1) or (2) on a discrete mesh is second-order-accurate in space and time. The two optional model algorithms, Eulerian [45] and semi-Lagrangian [44], correspond to Equations (1) and (2). Either algorithm can be written in the compact form

$$\psi_{\mathbf{i}}^{n+1} = LE_{\mathbf{i}}(\tilde{\psi}) + 0.5\Delta t R_{\mathbf{i}}^{n+1} \tag{3}$$

Here and throughout the remainder of this section, we drop the overbar for the transformed time coordinate to simplify notation; all t's are to be understood as $\bar{t}'$s. We denote $\psi_{\mathbf{i}}^{n+1}$ as the solution at the grid point $(\bar{\mathbf{x}}_{\mathbf{i}}, t^{n+1})$; $\tilde{\psi} \equiv \psi^n + 0.5\Delta t R^n$; and LE denotes either an advective semi-Lagrangian or a flux-form Eulerian NFT transport operator. In the Eulerian scheme, LE integrates the homogeneous transport Equation (1), i.e. LE advects $\tilde{\psi}$ using a fully second-order-accurate multidimensional NFT advection scheme (cf. Reference [40]). In the semi-Lagrangian algorithm, LE remaps transported fields arriving at the grid points $(\bar{\mathbf{x}}_{\mathbf{i}}, t)$ back to the departure points of the flow trajectories $(\bar{\mathbf{x}}_o(\bar{\mathbf{x}}_{\mathbf{i}}, t^{n+1}), t^n)$. Interestingly, the Lagrangian LE is also composed from NFT advection schemes. In contrast to the Eulerian case, however, it exploits directionally split 1D NFT advection schemes. The theory underlying such a design relies on elementary properties of differential forms [44, 43].† In technical terms, the semi-Lagrangian LE advects $\tilde{\psi}$ with a constant advective velocity on a local stencil in the vicinity of the departure point. This advective velocity is really a normalized displacement of the departure point to its nearest grid point, and can be different for each arrival point $(\bar{\mathbf{x}}_{\mathbf{i}}, t^{n+1})$ in Equation (3). Because of the latter, the semi-Lagrangian LE operator is not conservative, but thanks to the constancy of the local advective velocity, it is free of splitting errors. This is particularly convenient, as it allows the construction of fully second-order-accurate NFT fluid models based on constant-coefficient 1D advection schemes.

Transporting the auxiliary field $\tilde{\psi}$ (rather than the fluid variable alone) is important for the accuracy and stability of FT approximations. In the semi-Lagrangian algorithm, transporting $\tilde{\psi}$ derives straightforwardly from the trapezoidal-rule approximation for the trajectory integral of Equation (2)

$$\psi_{\mathbf{i}}^{n+1} = \psi_o + \int_T R d\tau \approx \psi_o + 0.5\Delta t(R_o + R_{\mathbf{i}}^{n+1}) \approx (\psi + 0.5\Delta t R)_o + 0.5\Delta t R_{\mathbf{i}}^{n+1} \tag{4}$$

where the subscript 'o' is a shorthand for the value at the departure point $(\bar{\mathbf{x}}_o(\bar{\mathbf{x}}_{\mathbf{i}}, t^{n+1}), t^n)$, and the second approximate equality accounts for eventual non-linearity of the LE remapping operator.

†An alternative argument employs the zeroth-order Taylor series expansion with higher-order accurate approximation of the first remainder that takes an integral form of the advection equation [43].

In the Eulerian algorithm, transporting $\tilde{\psi}$ is a consequence of correcting for the first-order truncation error proportional to the divergence of the advective flux of R. To show this, we first rewrite Equation (1) in a simpler form

$$\frac{\partial \rho^* \psi}{\partial t} + \bar{\nabla} \cdot (\tilde{\mathbf{u}} \psi) = \rho^* R \tag{5}$$

where $\tilde{\mathbf{u}} \equiv \rho^* \bar{\mathbf{v}}^* = \rho_b \bar{G} \dot{\bar{\mathbf{x}}}$. We assume a temporal discretization of Equation (5) in the form

$$\frac{\rho^{*n+1}\psi^{n+1} - \rho^{*n}\psi^n}{\Delta t} + \bar{\nabla} \cdot (\tilde{\mathbf{u}}^{n+1/2} \psi^n) = \rho^{*n+1/2} R^{n+1/2} \tag{6}$$

where $n + 1/2$ superscript denotes an $\mathcal{O}(\Delta t^2)$ accurate approximation for a field value at $t = t^n + 0.5\Delta t$, yet to be specified. The lack of temporal centring of the transported field ψ in the second term on the left-hand side (LHS) of Equation (6) is the defining property distinguishing FT schemes from CTS methods. With a straightforward (centred) higher-order discretization of the spatial derivatives, the differencing in Equation (6) leads typically to computationally unstable schemes; for example, consider the classical Euler-forward discretization for the constant coefficient, homogeneous case of Equation (6).

In order to arrive at a stable, fully second-order-accurate, and robust NFT algorithm, we proceed in the spirit of the one-step Lax–Wendroff schemes [17]: first, we evaluate the complete $\mathcal{O}(\Delta t)$ truncation error (due to uncentred time differencing) in terms of spatial differences; then, to compensate for this error, we add appropriate terms on the RHS of Equation (6) [48]. These terms are of two distinct types. The first is due solely to advection and must be compensated, by design, in any second-order-accurate FT advection scheme. The second term is related to implementation of the FT schemes in inhomogeneous advection problems. It appears in those 'naive' approximations to Equation (1) that simply combine an FT advection scheme for homogeneous transport with an $\mathcal{O}(\Delta t^2)$ approximation of $\mathrm{RHS}^{n+1/2}$. Ignoring this error leads to spurious $\sim \mathcal{O}(\Delta t)$ sinks/sources of 'energy' ψ^2 and, eventually, to non-linear instability (Appendix A in Reference [45]). Compensating this error to $\mathcal{O}(\Delta t^2)$ only requires subtracting a first-order-accurate approximation from the RHS of Equation (6).

The basic MPDATA algorithm is based upon a *time-independent* coefficient ρ^*. For time variable ρ^*, it is possible to generalize the algorithm and subtract additional error correction terms from the RHS of Equation (6) so as to still maintain an $\mathcal{O}(\Delta t^2)$ approximation [39] [14]. However there is an easier and more elegant alternative that works for any second-order-accurate time-independent-coefficient NFT flux-form advection scheme for a homogeneous Equation (6). Assuming a trapezoidal-rule approximation on the RHS of Equation (6)

$$\rho^{*n+1/2} R^{n+1/2} = 0.5(\rho^{*n} R^n + \rho^{*n+1} R^{n+1}) \tag{7}$$

and rearranging the homogeneous time-independent coefficient version of Equation (6) into the form

$$\psi_{\mathbf{i}}^{n+1} = \mathscr{A}_{\mathbf{i}}(\psi^n, \tilde{\mathbf{u}}^{n+1/2}, \rho^*) \equiv \psi_{\mathbf{i}}^n + \rho^{*-1} \Delta_{\mathbf{i}} \mathbf{F}(\psi^n, \tilde{\mathbf{u}}^{n+1/2}, \rho^*) \tag{8}$$

where $\Delta_{\mathbf{i}}\mathbf{F}$ symbolizes the difference of local advective fluxes that define the NFT scheme at hand then, the algorithm

$$\psi_{\mathbf{i}}^{n+1} = \frac{\rho^{*n}}{\rho^{*n+1}} \mathscr{A}_{\mathbf{i}}(\psi^n + 0.5\Delta t R^n, \tilde{\mathbf{u}}^{n+1/2}, \rho^{*n}) + 0.5\Delta t R_{\mathbf{i}}^{n+1} \tag{9}$$

approximates the solution to governing Equation (5) to the second-order accuracy. Identifying the first term on the RHS of Equation (9) with the *LE* operator on the RHS of Equation (3) closes the derivation of an Eulerian option of the NFT algorithm.

The congruence of the semi-Lagrangian and Eulerian options of the NFT approach in Equation (3) is convenient for applications. It allows for a fairly simple yet effective design of fluid models with optional use of either algorithm selectable by the user. Both options have merits, and in fact simulating the same physical problem with two different numerical algorithms helps to assess the significance of the truncation error [49]. Semi-Lagrangian advection schemes are not subject to the Courant–Friedrichs–Lewy (CFL) stability condition, thereby allowing for large-time-step integrations for smooth flows with small values of Lipschitz number $\mathscr{L}$. But, because of the topological concerns, the unconditional stability of semi-Lagrangian advection offers little advantage for simulating turbulent flows; cf. References [44, 2, 31]. Since the flux-form of the Eulerian schemes assures local conservation and accurate representation of Neumann boundary conditions [6], it leads, ultimately, to more suitable NFT schemes for simulating high-Reynolds-number flows. In general, however, the overall accuracy of the two options is problem-dependent [47], and there is no simple assessment valid throughout the entire range of geophysical applications. A hint of distinct behavioural errors [35] may be seen in Figure 2, where VLES simulations of the decaying turbulence result in larger values of entrophy for the Eulerian option of the model, while resolved DNS simulations yield the same values for both options.

4. AN ANELASTIC FLUID MODEL

4.1. Motivation

Up to now, we have carried out our discussion in abstraction from any particular system of fluid equations. While the NFT methods outlined in preceding sections can be directly applied to explicit integrations of a fully compressible Euler system,[†] because of the enormous span of the spatial and temporal scales important in geophysical fluids, explicit integrations of generic compressible equations are impractical (viz. prohibitively expensive) for most applications. As a result, meteorological models utilize a variety of analytic/numerical approximations to the fluid equations (hydrostatic, elastic, anelastic, Boussinesq, and so on; and evince many split-explicit or semi-implicit methods) for their integrations.

For research studies of all-scale turbulent geophysical fluids, we have found the anelastic non-hydrostatic system optimal so far. The anelastic equations may be viewed as combining two distinct approximations in the compressible Euler equations: a Boussinesq type linearization of the pressure gradient forces and mass fluxes in momentum and mass continuity equations, respectively; and the anelasticity *per se* equivalent to taking the limit of an infinite speed of sound. Although the anelastic equations were proven accurate for modelling weakly-stratified deep fluids, our recent results [49] document that the anelastic equations can capture adequately a broad range of planetary flows (i.e. shallow stratified fluids) while requiring relatively minor overhead due to the non-hydrostatic formulation. The adequacy of the anelastic approximation has important practical consequences. The Boussinesq linearization inherent

[†]See Reference [45] for a hydraulic analogy.

in the anelastic system greatly simplifies the task of designing accurate, flexible, and computationally efficient 'all-scale-research' models for meteorological circulations. This is especially important within the class of NFT models, where two-time-level self-adaptive non-linear numerics leads inevitably to difficult non-linear elliptic problems for implicit discretizations of fully compressible Euler equations.

4.2. *Analytic formulation*

A unique feature of our mathematical model is that it has the flexibility to solve the governing equations in a variety of domains. The capability for this flexibility comes from a generalized coordinate transformation, or *homeomorphism*, that maps the physical domain $(\mathbf{x}, t)$ where $\mathbf{x} \equiv (x, y, z)$—into a transformed, computational domain $(\bar{\mathbf{x}}, \bar{t})$ where $\bar{\mathbf{x}} \equiv (\bar{x}, \bar{y}, \bar{z})$. Thus the physical and transformed spaces share the same topological properties, such as connectivity. The physical space must be *Riemannian* [50] so that the *fundamental* (or *distance*) *metric* is defined (which does not have to be positive definite in anticipation of relativistic applications). An added, extremely powerful capability that is enabled by the mapping technique is *Dynamic Grid Adaptation* (DGA). DGA allows the computational grid to deform so as to follow features of interest in an evolving solution. The DGA capability is enabled by moving the numerical grid along coordinate isolines. The widespread use of coordinate mapping for grid adaptation in the engineering community dates back to a seminal paper by Thompson *et al*. [51] and is approaching a status as a mature subfield in computational fluid dynamics. Although the use of coordinate mapping for grid adaptation also dates back to nearly the same time in the meteorological community [10], it has not been as widely embraced; recent works include References [8, 31, 9, 34, 14].

Transformation overview. The three dimensional, time variable mapping is given by

$$(\bar{t}, \bar{x}, \bar{y}, \bar{z}) = (t, E(t, x, y), D(t, x, y), C(t, x, y, z)) \tag{10}$$

Note that in particular $(\bar{x}, \bar{y})$ do not depend upon the vertical coordinate z. This keeps vertical columns vertical and considerably simplifies the number of metric terms that appear.

Generalized transport equations. The anelastic model equations for moist convection [21] form the basis of our model, which are then further modified by subtracting off a specified environmental state. The resulting 'perturbation' equations (we actually end up solving for full velocity, perturbation potential temperature, and ultimately, perturbation pressure) in physical space are transformed utilizing the mapping functions defined in Equation (10). Following the basic form already laid out in Equation (1), the resulting continuity, momentum, and potential temperature equations (for extensions to moist processes, see Reference [12]) may be written as

$$\bar{\nabla} \cdot (\rho^* \bar{\mathbf{v}}^s) = 0 \tag{11}$$

$$\frac{\mathrm{d}\mathbf{v}}{\mathrm{d}\bar{t}} = \mathbf{F}_p + \mathbf{g}\theta'/\theta_b + \mathbf{F}_{oth} \tag{12}$$

$$\frac{\mathrm{d}\theta'}{\mathrm{d}\bar{t}} = F_\theta - \overline{\mathbf{v}^s} \cdot \bar{\nabla}\theta_e \tag{13}$$

where the jth component ($j=1,2,3$ corresponding to the $\bar{x},\bar{y},\bar{z}$ components, respectively) of the pressure gradient force is given by

$$F_p^j = \sqrt{g^{jj}}\left(E_{,x^j}\frac{\partial\pi'}{\partial\bar{x}} + D_{,x^j}\frac{\partial\pi'}{\partial\bar{y}} + C_{,x^j}\frac{\partial\pi'}{\partial\bar{z}}\right) \tag{14}$$

Equations (11)–(13) need to be studied carefully—while they look more or less like the standard forms there are a few subtleties involved. The differential operators $\bar{\nabla}$ and $\mathrm{d}/\mathrm{d}\bar{t}$, and the contravariant velocity $\overline{\mathbf{v}^*}$ have already been defined in Section 3. Appearing in the continuity (11) and potential temperature (13) equations is the *solenoidal velocity*, $\overline{\mathbf{v}^s} \equiv \overline{\mathbf{v}^*} - \partial\bar{\mathbf{x}}/\partial t$, so named because of the form continuity Equation (11) takes with it. Note that Equation (11) is a completely general result for the transformation (10) provided that: (i) $\rho_b = \rho_b(\mathbf{x})$, i.e. the reference density field is time-independent; and (ii) the physical coordinate system $\mathbf{x}$ is also time-independent (Cartesian, cylindrical, spherical, oblate spheroidal, and so on, would all be acceptable choices for the physical system). A proof for the form Equation (11) is outlined in the Appendix of Reference [34]. In the momentum equation, it is the *physical velocity* $\mathbf{v}$, defined in the *physical coordinates* $\mathbf{x}$, that is advected by the material derivative. Thus Equations (11)–(13) use three distinct sets of velocities. Note that in general, only the physical velocity $\mathbf{v}$ will have the dimension of velocity (e.g., units of ms^{-1}). A distinct physical velocity, $\bar{\mathbf{v}}$, also exists for the transformed coordinate system $\bar{\mathbf{x}}$. Using tensor notation, it is given by $\overline{v^j} = \overline{v^{*j}}\sqrt{\overline{g_{jj}}}$ where summation is not implied on the indices. Now assuming the usual summation convention, the contravariant velocity is written as $\overline{v^{*j}} = (\partial\overline{x^j}/\partial x^k)v^{*k}$ (with $k=0,1,2,3$—$k=0$ referring to time [34]), and the diagonal elements of the metric tensor of the transformed coordinates are $\overline{g_{jj}} = g_{pq}(\partial x^p/\partial\overline{x^j})(\partial x^q/\partial\overline{x^j})$. The metric and conjugate metric tensors for the physical coordinate system (which need not be Cartesian) are g_{pq} and g^{pq}, respectively. The Jacobian of the mapping into the transformed coordinate system is $\bar{G} = |\overline{g_{pq}}|^{1/2}$. The physical $\overline{v^j}$ and contravariant $\overline{v^{*j}}$ velocity thus differ by the scale factor $\sqrt{\overline{g_{jj}}}$. The physical velocities $\bar{\mathbf{v}}$ and $\mathbf{v}$ are identical, but their components are aligned with different coordinate systems ($\bar{\mathbf{x}}$ and $\mathbf{x}$, respectively). Our experience has been that it is easier to work with $\mathbf{v}$ and hence we have excluded $\bar{\mathbf{v}}$ from the algorithm *by design*.

Forcings in the momentum Equation (12) due to perturbations from the environmental state, such as Coriolis and centrifugal forces due to rotations and Christoffel symbols, and frictional/stress terms such as damping (e.g. gravity-wave absorbers in vicinity of open boundaries) and/or SGS modelling are all included in the $\mathbf{F}_{oth}$ term. $\mathbf{g} \equiv (0,0,g)$ is the acceleration of gravity. The F_θ term in the potential temperature equation corresponds to any thermal forcing—such as radiation, damping and/or SGS modelling terms. Subscripts 'b' and 'e' refer to the basic and environmental states, respectively—references which are particularly suitable for geophysical flows. Finally, $\theta' = \theta - \theta_e$, $\pi' = (p - p_e)/\rho_b$, and subscripts '$,x^j$' appearing in Equation (14) denote partial differentiation.

Reference states. The basic state directly associated with the anelastic approximation is in *hydrostatic balance*, and: it is (i) steady; (ii) it has the flow $\mathbf{V}_b = (u_b(z),0,0)$; (iii) it satisfies the equation of state, $p_b = \rho_b R T_b$; and (iv) it has potential temperature, pressure and density fields $\theta_b(z) = \theta_{ref}\exp[(z - z_{ref})/H_\theta]$, $p_b(z)$, and $\rho_b(z)$, respectively. The basic state satisfies only the pressure gradient and buoyancy forcings. Subtraction of the basic state equations from

the full form of the compressible fluid equations, together with the Boussinesq linearization of the pressure gradient forces and mass fluxes, leads to the anelastic system, which has the merit of filtering out sound waves while allowing thermal compressibility effects [21]. Since the coordinate mapping is time-variable, the transient term must be retained in the contravariant form of anelastic continuity [31, 34]—motivating the use of the solenoidal velocity in Equation (11).

The environmental state is a solution of the anelastic system that minimally satisfies *geostrophic balance*, e.g. terms arising from Coriolis and centrifugal forces due to rotation and Christoffel symbols. We assume this state (i) is steady, (ii) has the flow $\mathbf{V}_e = (u_e(y,z), v_e(y,z), 0)$, (iii) satisfies the equation of state, and (iv) has potential temperature, pressure, and density fields $\theta_e(y,z)$, $p_e(y,z)$, and $\rho_e(y,z)$, respectively. In addition to the geostrophic terms, the environmental state may satisfy a thermal forcing term that perturbs the potential temperature from its basic state value.

4.3. Numerical implementation

Equations (12) and (13) are solved implicitly for the physical velocity, **v**, and potential temperature perturbation, θ', respectively; using Equation (3) as given in Section 3. Coriolis and centrifugal accelerations arising from rotation and Christoffel symbols, condensation, pressure gradients, and gravity-wave absorbers are all treated implicitly in the $R_{\mathbf{i}}^{n+1}$ term of Equation (3). SGS terms and slow phase-change tendencies (such as rain formation or evaporation [12]) are treated explicitly. The implicitness of the gravity-wave absorbers and the potential temperature enhance stability and accuracy. The implicitness of the pressure gradient forces is an essential feature as it enables the projection of the preliminary values of $LE(\tilde{\psi})$ onto solutions of the continuity Equation (11)—see Reference [5]. To make this projection, the system of simultaneous equations resulting from Equation (3) are algebraically inverted to construct expressions for the solenoidal velocity components. These components are substituted into Equation (11) producing an elliptic equation for pressure. This elliptic equation is solved (subject to appropriate boundary conditions) using the generalized conjugate-residual approach—a preconditioned non-symmetric Krylov solver (see References [46, 47], and the Appendix of Reference [49] for further details). Updated values of the physical velocity are then computed from the solenoidal velocities using the relation $v^j = \sqrt{g_{jj}}(\partial x^j/\partial \overline{x^p})\overline{v^s}^p$ where $p = 1, 2, 3$ (summation is implied in p index but not j). Finally, updated contravariant velocity components required for the material derivative appearing in Equation (12) are constructed from the solenoidal velocity according to $\overline{v^*}^j = \overline{v^s}^j + \overline{x^j}_{,t}$.

5. GRAVITY-WAVE INDUCED TURBULENCE AT MESOPAUSE ALTITUDES

This problem is of interest for at least two reasons. First, the middle atmosphere is known to be far from radiative equilibrium at mesopause altitudes and wave forcing is the main factor behind this phenomenon [11]. Determination of the extent to which gravity wave breaking is responsible for this non-equilibrium has great relevance to a complete understanding of the wave forcing and its parameterization. Second, numerical simulation of turbulence is of considerable theoretical interest. The wave breaking in this study generated a highly inhomogeneous, anisotropic turbulence. It was not initialized according to any *a priori* turbu-

lence model nor constrained by domain size (which can limit wave–wave interactions, see Reference [37]). Instead, the turbulence developed from a very smooth linear wavefield in accord with the physics of a wave packet propagating into a very deep model atmosphere (of over 16 density scale heights—corresponding to a density variation from the bottom to the top of over 10^7 to one).

5.1. Model setup

This experiment was run using the semi-Lagrangian option of the model in a massively parallel mode on a 512 processor Cray T3E (see Reference [34]). It simulated the evolution of an internal gravity wave packet generated by a narrow, 2D squall line at tropopause levels (~ 15 km altitude) and its subsequent breaking near the mesopause (~ 85 km altitude) using a mesoscale sized, Cartesian physical domain. We used a spatio-temporal Gaussian deflection of the lower domain boundary (streamline) as a proxy for the squall line disturbance. The transformed vertical coordinate was prescribed as the time variable generalization [31] of terrain following coordinates [10]—$\bar{z} \equiv C(t,x,y,z) = H(z - z_s)/(H - z_s)$ where $z_s \equiv z_s(t,x,y) = A \exp[-((x - x_{ref} + c_x t)/\sigma_x)^2] \exp[-((t - t_{ref})/\sigma_t)^2]$. The values of the various parameters were: $A = 200$ m, $x_{ref} = -30$ km, $c_x = 7$ ms^{-1}, $\sigma_x = 2$ km, $t_{ref} = 2$ h, and $\sigma_t = 1$ h [31]. Although the horizontal coordinates were not stretched, this test case clearly illustrates the time variable coordinate stretching capability that is inherent in the model.

The basic state (the environmental state was set identically) was one of uniform zonal wind ($u_b = -32$ ms^{-1}), stability (with Brunt–Väisällä frequency $N = 0.02$ s^{-1}), and density scale height (e.g. $\rho_b(z) = \rho_{ref} \exp(-(z - z_{ref})/H_\rho)$ with $H_\rho = 6.63$ km). These conditions initially favour the development of a 2D wavefield that is monochromatic, quasi-stationary, and has near unity aspect ratio. Each of these characteristics is due to linear wave dispersion. A few Brunt–Väisällä periods after maximum forcing, this wavefield undergoes a 2D primary (convective) instability [31].

The computational grid consisted of $544 \times 80 \times 291$ (zonal $\times$ spanwise $\times$ vertical) points with a resolution of 380 m.[§] To save computer resources, the problem was executed in 2D on a $544 \times 1 \times 291$ grid with a timestep of $\Delta t = 5.0$s until 120 minutes of the physical time. At 120 minutes, the 3D domain was created by repeating the solution in the spanwise direction y, and seeding the buoyancy field with a small amplitude ($< 1\%$ of the basic state) white noise. The time chosen for 3D seeding was carefully selected based upon data generated with earlier 2D [31] and 3D [32] experiments. Further computations continued in 5 minute portions of physical time using a timestep of $\Delta t = 2.5$ s. The run was terminated at 180 minutes because at this point breaking had consumed the zonal extent of the domain. The lateral zonal and spanwise boundaries were periodic with lateral zonal sponges.

A specially tuned vertical sponge was employed, such that it approximated the effects of atmospheric viscosity for waves resulting from the primary instability. Explicit SGS dissipation was not employed in this simulation. Instead, energy removal at the grid scale was effected with the monotonicity option of the semi-Lagrangian interpolator. As discussed in Section 2, this option invokes a topological constraint whereby no two streamtubes are allowed to intersect. Interestingly, this flow realizability condition was observed to be equivalent to a second

[§]A truncation error study reported in Reference [31] for the 2D primary instability indicates that 625 m resolution is adequate to capture the correct morphological development in wavebreaking.

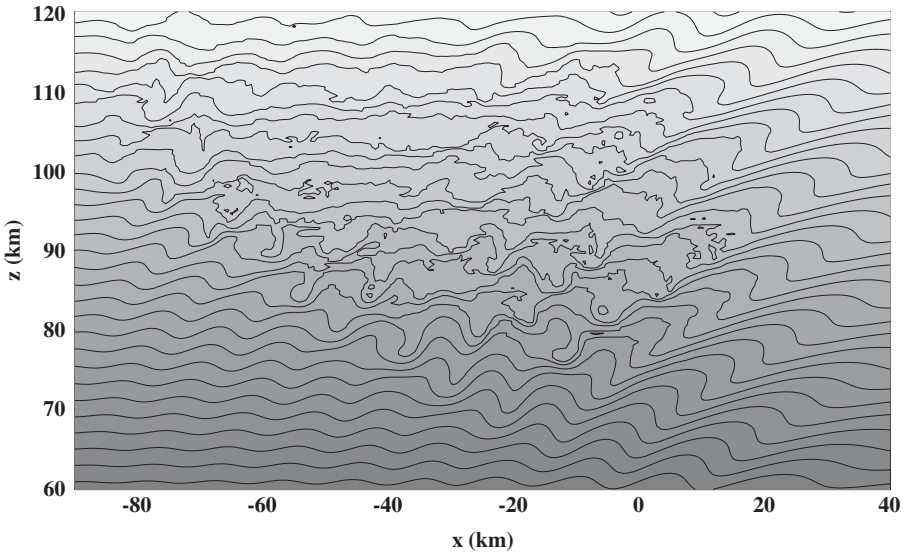

Figure 3. Results from the wavebreaking experiment: contour density plot of $\ln(\theta)$ in vertical xz (zonal) plane at spanwise location $y = 0$ km at $t = 155$ minutes showing region of vigorously breaking waves.

law constraint—the energy removal at the grid scale occurred at just the rate needed to avoid local negative entropy production [31] (which was easily monitored by observing the evolution of the θ field). Atmospheric viscosity (which varies approximately as ρ^{-1}) is sufficiently large near the domain top that the Kolmogorov microscale was the same order of magnitude as the grid size at the initial altitude of breaking and the simulation in this upper region was effectively DNS. Well below this altitude, however, atmospheric viscosity is many orders of magnitudes smaller and in this region the simulation should be considered VLES.

5.2. *Results*

Some idea of the inhomogeneity of the wavefield can be gleaned from Figures 3 and 4, which show contour density plots of the potential temperature (θ) field. The vertical plane of Figure 3 is parallel to the zonal flow, whereas the vertical plane of Figure 4 is perpendicular to the zonal flow. In Figure 3 the wavefield is clearly seen to be inhomogeneous in both the vertical and zonal (left to right) directions, whereas from Figure 4 the wavefield can be observed to be homogeneous in the spanwise direction (left to right). Note that the complete altitude range $15 \leqslant z \leqslant 125$ km is not shown in these figures; the regions above and below that shown are very smooth and characterized by almost constant stratification. The anisotropy and evolution of the turbulence were assessed by examining (i) velocity derivative skewness [33], and (ii) 1D and 2D energy spectra computed from θ fields;¶ see [34] for details regarding the computations of the spectra.

¶Approximate equipartition occurs even during wave breaking [32].

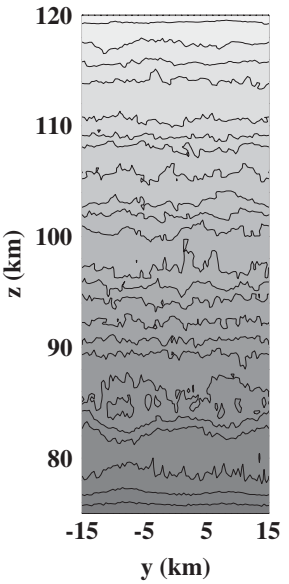

Figure 4. Contour density plot of $\ln(\theta)$ in vertical yz (spanwise) plane at zonal location $x = -35\,\mathrm{km}$ at $t = 155$ minutes showing region of vigorously breaking waves (same contour interval as in Figure 3).

Figure 5 shows the evolution of the zonal energy spectra. At 125 minutes energy is concentrated in a fundamental mode at $k = 0.40\,\mathrm{km}^{-1}$ ($\ln(k) = -0.90$), corresponding to $\lambda_x = 15.5\,\mathrm{km}$. At $k = 0.80\,\mathrm{km}^{-1}$ ($\ln(k) = -0.23$) a much weaker second harmonic—a harbinger of the primary convective instability that is about to occur—may be seen. The very sharp drop off between the fundamental and second harmonic is due to an evanescent wave limit at $k = 0.62\,\mathrm{km}^{-1}$. At later times wave dispersion causes the fundamental to broaden and peak at lower wavenumbers (longer waves are slower and take more time to propagate upwards—see Reference [31]. With the onset of vigorous wave overturning (~ 140 minutes), a buoyancy subrange [54] with a slope of -3 appears just upscale of the fundamental. Until this primary instability occurs, there is negligible energy at the highest wavenumbers. With the onset of a secondary (3D) instability, a tendency towards a $-5/3$ slope can be seen. The critical buoyancy wavenumber (Ozmidov scale) that separates the two regimes decreases from $k_b = 4.0$ to $1.8\,\mathrm{km}^{-1}$ as t increases from 140 to 180 minutes, respectively. This compares favourably with earlier results on a Cray J90 (at 625 m resolution) which yielded $k_b = 2.1\,\mathrm{km}^{-1}$ at 150 minutes [32]. The experimental value of k_b may also be compared with the scaling result, $k_b \sim N^3/\varepsilon_d \sim 1.6\,\mathrm{km}^{-1}$ [54], where ε_d is the turbulence dissipation rate. Finally Figure 5 shows another $-5/3$ power law regime at the lowest wavenumbers at earlier times (125 to 145 minutes). This is consistent with a 2D reversed energy cascade that is transferring energy into the zonal mean fields [16]. The Eliassen–Palm flux divergence has its maximum value precisely in this time interval, of order $0.02\,\mathrm{ms}^{-1}$, at breaking altitudes. After 150 minutes, the energy spectra flatten out at the lowest wavenumbers. At this point wave breaking has disrupted the linear wave field sufficiently that it lacks the larger scale coherence needed to effectively modify the zonal average state.

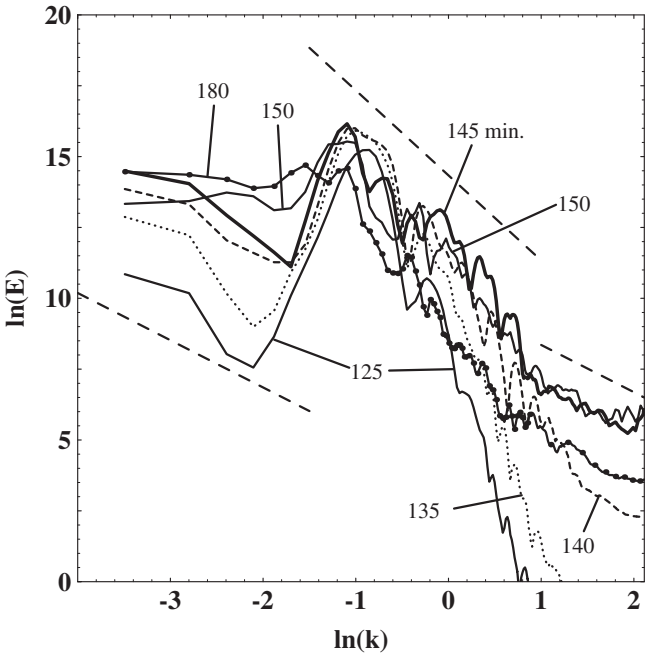

Figure 5. Time evolution of zonal spectral energy at 100 km altitude (straight dashed lines have slopes of $-5/3$ and -3).

Vertical spectra (not shown) show very similar evolutionary tendencies, with the only significant difference being a lack of the $-5/3$ power law regime at the lowest wavenumbers. Spanwise energy spectra (not shown) show very different evolutionary tendencies, however. The spectrum at 125 minutes is quite flat and 15 orders of magnitude below the fundamental of the zonal spectra. Growth of spanwise energy is negligible for the first 10–15 minutes after the 3D seeding. In the next 5–10 minutes spanwise spectral energy explodes as the secondary instability undergoes a period of exponential growth. An inertial subrange, characterized by a $-5/3$ power law appears at the highest wavenumbers. As t continues to increase, this subrange expands to lower wavenumbers, until at 180 minutes, most of the spectrum lies within it.

6. REMARKS

LES models and their attendant SGS schemes have become widely accepted as perhaps the best way to model turbulent flows with so many degrees of freedom that they are hopelessly beyond the possibility of DNS—a usage in marked contrast to their original application for removal of non-linear instability. The need to express the SGS terms as functions of the resolved eddy field makes the closure problem for SGS schemes mathematically not well posed (see Chapter XII.2.2 in Reference [19]), and there is no rigorous theory at present for constructing closures of the three-dimensional Navier–Stokes equations [15]. One way out of

this conundrum is to make certain assumptions (such as isotropy) about the nature of the fine scale turbulence being modelled by the SGS scheme.

Our gravity wave simulations (Section 5) clearly show that correct, *a priori*, assumptions about the nature of a geophysical turbulence can be difficult to make. In our example, the use of a standard assumption like isotropy could be detrimental as (i) the flow is strongly non-stationary, (ii) inhomogeneous, and (iii) shows *both* upscale and downscale energy flow. Regions of isotropic turbulence do exist, but they are complicated functions of spatial position and time.

An alternative to the SGS closure conundrum is to recognize that the SGS model is, in practice, a way to effect numerical stability. No attempt is made to determine what kind of information may 'lie' unresolved at the sub-grid scales. If an inverse cascade is not sufficiently resolved, it will not appear in the simulation. This is the idea behind VLES, and it immediately shifts the goals from those of developing fine scale turbulence models to those of effecting stability as sharply as possible (i.e. with minimum dissipative impact on the computation). This may appear to be a bit of a paradigm shift—from a physical viewpoint (for conventional LES models) to a mathematical/computational one (for VLES). But our development shows that sharp requirements for stability inevitably appear based in physics (see the discussion on flow topology and Lipschitz-number, $\mathscr{L}$, in Section 2; and the negative entropy generation argument from the gravity wave results in Section 5.1).

In inviscid or almost inviscid applications, these NFT schemes develop an implicit SGS model that applies the minimum dissipation needed to keep the computation stable. In non-stationary and/or inhomogeneous applications, the implicit SGS model 'self-adapts' to apply the dissipation smartly, only when and where it is needed. In conclusion, the NFT methods outlined and applied in this study can provide competitive (and in our examples superior) alternatives to standard LES methods, when used in the spirit of VLES.

APPENDIX A

In order to illustrate the enhanced computational stability of NFT advection schemes (sign-preserving, at least), consider a homogeneous continuity equation

$$\frac{\partial \psi}{\partial t} + \sum_{I=1}^{M} \frac{\partial}{\partial x^I}(\psi u^I) = 0 \tag{15}$$

where $\psi(\mathbf{x},t)$ is a constant-sign scalar field, and u^I is the Ith component of an arbitrary solenoidal flow.[‖] A corresponding flux-form advection algorithm can be compactly written as

$$\psi_{\mathbf{i}}^{n+1} = \psi_{\mathbf{i}}^{n} - \sum_{I=1}^{M} (F^I_{\mathbf{i}+1/2\mathbf{e}_I} - F^I_{\mathbf{i}-1/2\mathbf{e}_I}) \tag{16}$$

where $F^I_{\mathbf{i}+1/2\mathbf{e}_I}\Delta X^I$ is an approximation to the I component of the integrated (over time step Δt) advective flux ψu^I, evaluated at $\mathbf{i}+1/2\mathbf{e}_I$ position on the grid; $\mathbf{e}_I$ denotes the unit vector

[‖] Here, we assume a constant fluid density merely for simplicity in the argument; extensions to variable densities (and/or geometries) follow the development in Section 3 of this paper.

in the I direction. For simplicity, assume that both analytic and numerical fluxes vanish at the boundaries of a computational domain. Then, the conservation form of Equation (16) implies

$$\forall n \sum_{\mathbf{i}} \psi_{\mathbf{i}}^{n} = \sum_{\mathbf{i}} \psi_{\mathbf{i}}^{0} \tag{17}$$

Since the scheme preserves the sign of the transported quantity by assumption, Equation (17) is equivalent to

$$\forall n \sum_{\mathbf{i}} |\psi_{\mathbf{i}}^{n}| = \sum_{\mathbf{i}} |\psi_{\mathbf{i}}^{0}| \tag{18}$$

Recalling that $\sum |\,| \geqslant (\sum (\,)^2)^{1/2}$, Equation (18) implies that

$$\forall n \sum_{\mathbf{i}} (\psi_{\mathbf{i}}^{n})^2 \leqslant \left(\sum_{\mathbf{i}} |\psi_{\mathbf{i}}^{0}| \right)^2 \equiv \mathscr{B} \tag{19}$$

In other words, total 'energy' of the sign-preserving solution is uniformly bounded in time, which is to say that the sign-preserving solution is computationally stable.

The simplicity of the result in Equation (19) is a direct consequence of the assumption that ψ is of a constant sign. For variable-sign fields, a similar result may be obtained by noting that any ψ may be uniquely decomposed into the non-positive and non-negative part, $\psi = [\psi]^+ + [\psi]^-$ with $[\psi]^+ \equiv \max(0, \psi)$ and $[\psi]^- \equiv \min(0, \psi)$. Since Equation (15) is equivalent to the Lagrangian form

$$\frac{\mathrm{d}\psi}{\mathrm{d}t} = 0 \tag{20}$$

(where $\mathrm{d}/\mathrm{d}t$ denotes the material derivative) and since $[\psi]^+$ and $[\psi]^-$ have disjoined supports along a flow trajectory, Equation (20) implies

$$\frac{\mathrm{d}[\psi]^+}{\mathrm{d}t} = 0, \quad \text{and} \quad \frac{\mathrm{d}[\psi]^-}{\mathrm{d}t} = 0 \tag{21}$$

whereupon both $[\psi]^+$ and $[\psi]^-$ must satisfy Equation (15). Applying a sign-preserving advection scheme to both parts ensures uniform boundedness of both $[\psi]^+$ and $[\psi]^-$, and consequently of their sum.

ACKNOWLEDGEMENTS

This work was supported in part by the Department of Energy 'Climate Change Prediction Program' (CCPP) research initiative, and by National Science Foundation grant #ATM 9616811. The use of the 512 PE Cray T3E at NERSC and of the 32 PE Cray T3E at ICM is gratefully acknowledged.

REFERENCES

1. Arakawa A. Computational design for long-term numerical integration of the equations of fluid motions: Two-dimensional incompressible flow. *Journal of Computational Physics* 1966; **1**:119–143.
2. Bartello P, Thomas SJ. The cost-effectiveness of semi-Lagrangian advection. *Monthly Weather Review* 1996; **124**:2883–2897.
3. Batchelor GK. *An Introduction to Fluid Dynamics*. Cambridge University Press: Cambridge, 1967.
4. Brown AR, MacVean MK, Mason PJ. The effects of numerical dissipation in large eddy simulations. *Journal of the Atmospheric Sciences* 2000; **120**:3337–3348.

5. Chorin AJ. Numerical solution of the Navier–Stokes equations. *Mathematical Computation* 1968; **22**:742–762.
6. Cullen M, Salmond D, Smolarkiewicz PK. Key numerical issues for future development of the ECMWF models. *Proceedings of ECMWF Workshop on Developments in Numerical Methods for Very High Resolution Global Models*, ECMWF, Reading, U.K., 2000; 183–206.
7. Deardorff JW. Sub-grid-scale turbulence modellings. In *Issues in Atmospheric and Oceanic Modeling*, *Part B. Weather Dynamics*, *Advances in Geophysics*, Saltzman B, Manabe S (eds). Academic Press: New York, 1985; 337–343.
8. Dietachmayer GS, Droegemeier KK. Application of continuous dynamic grid adaptation techniques to meteorological modelling. Part 1: Basic formulation and accuracy. *Monthly Weather Review* 1992; **120**: 1675–1706.
9. Fox-Rabinovitz MS, Stenchikov GL, Suarez MJ, Takacs LL, Govindaraju RC. A uniform- and variable-resolution stretched-grid GCM dynamical core with realistic orography. *Monthly Weather Review* 2000; **128**:1883–1898.
10. Gal-Chen T, Somerville CJ. On the use of a coordinate transformation for the solution of the Navier–Stokes equations. *Journal of Computational Physics* 1975; **17**:209–228.
11. Garcia RR, Solomon S. The effects of breaking gravity waves on the dynamics and chemical composition of the mesosphere and lower thermosphere. *Journal of Geophysical Research* 1985; **90**:3850–3868.
12. Grabowski WW, Smolarkiewicz PK. On two-time level semi-Lagrangian modelling of precipitating clouds. *Monthly Weather Review* 1996; **124**:487–497.
13. Herring JR, Kerr RM. Development of enstrophy and spectra in numerical turbulence. *Physics of Fluids A* 1993; **5**:2792–2798.
14. Iselin JP, Prusa JM, Gutowski WJ. Dynamic grid adaptation using the MPDATA scheme. *Monthly Weather Review* 2001; in press.
15. Kosović B. Subgrid-scale modelling for large-eddy simulation of high-Reynolds-number boundary layers. *Journal of Fluid Mechanics* 1997; **336**:151–182.
16. Kraichnan RH. Inertial ranges in two-dimensional turbulence. *Physics of Fluids* 1967; **10**:1417–1423.
17. Lax P, Wendroff B. System of conservation laws. *Communications on Pure and Applied Mathematics* 1960; **13**:217–237.
18. Lesieur M, Metais O. New trends in LES of turbulence. *Annual Review of Fluid Mechanics* 1996; **28**:45–82.
19. Lesieur M. *Turbulence in Fluids*. Kluwer: New York, 1997.
20. Linden PF, Redondo JM, Youngs DL. Molecular mixing in Rayleigh–Taylor instability. *Journal of Fluid Mechanics* 1994; **265**:97–124.
21. Lipps FB, Hemler RS. A scale analysis of deep moist convection and some related numerical calculations. *Journal of the Atmospheric Sciences* 1982; **39**:2192–2210.
22. Margolin LG, Smolarkiewicz PK, Sorbjan Z. Large-eddy simulations of convective boundary layers using non-oscillatory differencing. *Physica D* 1999; **133**:390–397.
23. Mason PJ. Large-eddy simulation: A critical review of the technique. *Quarterly Journal of the Royal Meteorological Society* 1994; **120**:1–35.
24. Moin P, Kravchenko AG. Numerical issues in large eddy simulations of turbulent flows. In *Numerical Methods for Fluid Dynamics VI*, Baines MJ (ed.). Will Print, 1998; 123–136.
25. Muschinski A. A similarity theory of locally homogeneous and isotropic turbulence generated by a Smagorinsky-type LES. *Journal of Fluid Mechanics* 1996; **325**:239–260.
26. Oran ES, Boris JP. Computing turbulent shear flows—a convenient conspiracy. *Computers in Physics* 1993; **7**:523–533.
27. Orszag SA, Staroselsky I. CFD: Progress and problems. *Computer Physics Communications* 2000; **127**: 165–171.
28. Ottino JM. *The Kinematics Of Mixing*: *Stretching*, *Chaos*, *And Transport*, Cambridge University Press: Cambridge, 1989.
29. Porter DH, Pouquet A, Woodward PR. Kolmogorov-like spectra in decaying three-dimensional supersonic flows. *Physics of Fluids* 1994; **6**:2133–2142.
30. Potter D. *Computational Physics*. Wiley: Chichester, 1973.
31. Prusa JM, Smolarkiewicz PK, Garcia RR. On the propagation and breaking at high altitudes of gravity waves excited by tropospheric forcing. *Journal of the Atmospheric Sciences* 1996; **53**:2186–2216.
32. Prusa JM, Garcia RR, Smolarkiewicz PK. Three-dimensional evolution of gravity wave breaking in the mesosphere. *Preprints 11th Conference on Atmospheric*, *Ocean and Fluid Dynamics*, American Meteorological Society, 1997; J3–J4.
33. Prusa JM, Smolarkiewicz PK, Wyszogrodzki AA. Parallel computations of gravity wave turbulence in the Earth's atmosphere. *SIAM News* 1999; **32**:1–12.
34. Prusa JM, Smolarkiewicz PK, Wyszogrodzki AA. Simulations of gravity wave induced turbulence using 512 PE CRAY T3E. *International Journal of Applied Mathematics and Computer Science* 2001; **11**(4):101–115.
35. Roache PJ. *Computational Fluid Dynamics*. Hermosa Publishers, 1972.
36. Schmidt H, Schumann U. Coherent structure of the convective boundary layer derived from large-eddy simulation. *Journal of Fluid Mechanics* 1989; **200**:511–562.

37. Scinocca JF. The mixing of mass and momentum by Kelvin–Helmholtz billows. *Journal of the Atmospheric Sciences* 1995; **52**:2509–2530.
38. Smagorinsky J. Some historical remarks on the use of non-linear viscosities. In *Large Eddy Simulation of Complex Engineering and Geophysical Flows*, Galperin B, Orszag SA (eds). Cambridge University Press: Cambridge, 1993; 3–36.
39. Smolarkiewicz PK. A fully multidimensional positive definite advection transport algorithm with small implicit diffusion. *Journal of Computational Physics* 1984; **54**:325–362.
40. Smolarkiewicz PK, Clark TL. The multidimensional positive definite advection transport algorithm: Further development and applications. *Journal of Computational Physics* 1986; **67**:396–438.
41. Smolarkiewicz PK. Comment on "A Positive Definite Advection Scheme Obtained by Nonlinear Renormalization of the Advective Fluxes". *Monthly Weather Review* 1989; **117**:2626–2632.
42. Smolarkiewicz PK. Nonoscillatory advection schemes. *Proceedings of ECMWF Workshop on Numerical Methods in Atmospheric Models*, ECMWF, Reading, U.K., 1991; 235–256.
43. Smolarkiewicz PK, Grell GA. A class of monotone interpolation schemes. *Journal of Computational Physics* 1992; **101**:431–440.
44. Smolarkiewicz PK, Pudykiewicz JA. A class of semi-Lagrangian approximations for fluids. *Journal of the Atmospheric Sciences* 1992; **49**:2082–2096.
45. Smolarkiewicz PK, Margolin LG. On forward-in-time differencing for fluids: Extension to a curvilinear framework. *Monthly Weather Review* 1993; **121**:1847–1859.
46. Smolarkiewicz PK, Margolin LG. Variational solver for elliptic problems in atmospheric flows. *Applied Mathematics and Computer Science* 1994; **4**:527–551.
47. Smolarkiewicz PK, Margolin LG. On forward-in-time differencing for fluids: An Eulerian/semi-Lagrangian nonhydrostatic model for stratified flows. *Atmospheric Ocean Special* 1997; **35**:127–152.
48. Smolarkiewicz PK, Margolin LG. MPDATA: A finite-difference solver for geophysical flows. *Journal of Computational Physics* 1998; **140**:459–480.
49. Smolarkiewicz PK, Margolin LG, Wyszogrodzki AA. A class of nonhydrostatic global models. *Journal of the Atmospheric Sciences* 2001; **58**:349–364.
50. Synge JL, Schild A. *Tensor Calculus*. Dover Press, 1949.
51. Thompson JF, Thames FC, Mastin CW. Automatic numerical generation of body-fitted curvilinear coordinate system for field containing any number of arbitrary two-dimensional bodies. *Journal of Computational Physics* 1974; **15**:299–319.
52. Tremback CJ, Powell J, Cotton WR, Pielke AR. The forward-in-time upstream advection scheme: Extension to higher orders. *Monthly Weather Review* 1987; **115**:540–555.
53. Truesdell C. *The Mechanical Foundations of Elasticity and Fluid Dynamics*. Gordon and Breach Science Publishers, Inc., 1966.
54. Weinstock J. Theoretical gravity wave spectrum in the atmosphere: Strong and weak wave interactions. *Radio Science* 1985; **20**:1295–1300.

